Structure and thermal decomposition of ammonium metatungstate

Dávid Hunyadi[1], István Sajó[2], Imre Miklós Szilágyi[1,3,*]

[1]Budapest University of Technology and Economics, Department of Inorganic and Analytical Chemistry, H–1111 Budapest, Szt. Gellért tér 4. Hungary;

[2]Environmental Analytical & Geoanalytical Research Group, Szentágothai Research Centre, University of Pécs, H-7624 Pécs, Ifjúság útja 20. Hungary;

[3]Technical Analytical Chemistry Research Group of the Hungarian Academy of Sciences, H–1111 Budapest, Szt. Gellért tér 4. Hungary

Corresponding author: imre.szilagyi@mail.bme.hu

Keywords

Ammonium metatungstate, TG/DTA, MS, XRD, FTIR

Abstract

The structure, morphology of ammonium metatungstate (AMT), $(NH_4)_6[H_2W_{12}O_{40}]\cdot 4H_2O$ and its thermal decomposition in air and nitrogen atmospheres were investigated by SEM, FTIR, XRD and TG/DTA-MS. The cell parameters of the AMT sample were determined and refined with a full profile fit. The thermal decomposition of AMT involved several steps in inert atmosphere: (i) release of crystal water between 25-200 °C resulting in dehydrated AMT; (ii) formation of an amorphous phase between 200-380 °C, (iii) from which hexagonal WO_3 formed between 380-500 °C, (iv) which then transformed into the more stable m-WO_3 between 500-600 °C. As a difference in air, the as-formed NH_3 ignited with an exothermic heat effect, and nitrous oxides formed as combustion products. The thermal behavior of AMT was similar to ammonium paratungstate (APT), $(NH_4)_{10}[H_2W_{12}O_{42}]\cdot 4H_2O$, the only main difference being the lack of dry NH_3 evolution between 170-240 °C in the case of AMT.

Introduction

Ammonium tungstates are important members of isopolytungstates. They have three forms, i.e. ammonium paratungstate (APT), $(NH_4)_{10}[H_2W_{12}O_{42}]\cdot xH_2O$ (X=4,7,10); ammonium metatungstate (AMT), $(NH_4)_6[H_2W_{12}O_{40}]\cdot nH_2O$ (n=1-22); and ammonium orthotungstate (AT), $(NH_4)_2WO_4$ [1]. One of their major applications is that tungsten oxides, metal tungstates, tungsten carbides or tungsten metal can be prepared from them, all of which are significant for various industries. Tungsten oxides can be used as catalysts [2-5], photocatalysts [6-10], gas sensors [11-18], chromogenic materials [19-21]; metal tungstates can be used among others as catalysts [22], pigments [23,24]; tungsten carbides are the hard components in cutting, drilling, tools [25-27] and they are also used as catalysts [28,29]; while tungsten metal is a key element in lighting industry [1,30-34].

The industrial preparation of tungsten oxides, tungsten carbides and tungsten metal is mostly based on thermal decomposition (oxidation or reduction) of ammonium tungstates. Among ammonium tungstates, only the thermal behavior of APT was studied in detail in the past decades, which is mostly explained by that APT with is well defined preparation route and structure is the starting material of tungsten manufacture [1,32,33]. In contrast, to the best of our knowledge, the thermal decomposition of AMT and AT has not been investigated in detail. This is unexpected, especially in the case of AMT, as it is the most water soluble ammonium tungstate, and AMT is widely used to prepare various tungsten oxide nanostructures by annealing [35,36].

In the case of AMT, not only its thermal decomposition sequence, but also is structure and composition are not straightforward. According to Christian and Wittingham [37] as well as Fait et al [38], depending on its crystal water content AMT can have three different cubic unit cells, however, only of them, the $AMT\cdot 22H_2O$ has an XRD reference card (PDF 00-039-0168). There exists a fourth, anorthic AMT structure (PDF 04-012-6600) as well. In addition, commercial AMT can be obtained with different CAS numbers (e.g. 12333-11-8, 402568-09-6, 12028-48-7), to which different compositions are assigned, i.e. $(NH_4)_6[H_2W_{12}O_{40}]\cdot nH_2O$ or $(NH_4)_6[W_{12}O_{39}]\cdot yH_2O$.

In the presents study, we aimed to get more information on the structure of AMT and intended to characterize its thermal decomposition. In addition, we compared the structure and thermal behavior of the commercially available AMT products. To achieve these, we studied the structure and morphology of the AMT materials and compared their thermal decomposition by scanning electron microscopy (SEM), Fourier transform infrared spectroscopy (FTIR),

powder X-ray diffraction (XRD) and thermal analysis (TG/DTA-MS) in inert (N_2) and in oxidizing (air) atmospheres.

Experimental

Two ammonium metatungstate samples were obtained from Sigma-Aldrich with compositions of $(NH_4)_6[H_2W_{12}O_{40}]\cdot nH_2O$ (CAS: 12333-11-8) and $(NH_4)_6[W_{12}O_{39}]\cdot yH_2O$ (CAS 402568-09-6), and they were named AMT1 and AMT2, respectively.

SEM images were obtained by a JEOL JSM-5500LV scanning electron microscope.

Powder XRD patterns were recorded on a PANalytical X'pert Pro MPD X-ray diffractometer using Cu K_α radiation.

FTIR spectra were measured by an Excalibur Series FTS 3000 (Biorad) FTIR spectrophotometer in the range of 400-4000 cm^{-1} in KBr pellets.

TG/DTA measurements were performed on an STD 2960 Simultaneous DTA/TGA (TA Instruments Inc.) thermal analyzer using a heating rate of 10 °C min^{-1} and Pt crucibles. The reactor was purged either with air or nitrogen atmospheres (130 ml min^{-1}). Evolved gas analytical (EGA) curves were recorded by a Thermostar GSD 200 (Balzers Instruments) quadruple mass spectrometer (MS). A mass range between m/z = 1-64 was monitored through 64 channels in Multiple Ion Detection Mode (MID) with a measuring time of 0.5 s $channel^{-1}$. Further details of the TG/DTA-MS setup are described elsewhere [39,40].

Results and discussion

Characterization of AMT1

According to SEM images (Fig. 1a), AMT1 consisted of ca. 5-50 μm microspheres. Many such spheres were cracked, and the empty inner part of the spheres could be seen, showing that AMT1 was actually built up by hollow microspheres. In the voids of cracked larger spheres, even smaller spheres could be seen, which could get inside most probably after the cracking occurred.

In the FTIR spectrum of AMT1 (Fig. 2a), the O-H deformation and stretching vibrations of water molecules in AMT were present around 1630 cm^{-1} and 3570 cm^{-1}, while the N-H deformation and stretching vibrations of NH_4^+ ions were visible at 1400 cm^{-1} and 3135 cm^{-1}. The peaks belonging to the metatungstate ion were observable mostly below 1000 cm^{-1},

which could be identified based on the FTIR data of pure polytungstates, AMT composites and WO_3 [36,41-45], as the FTIR spectrum of AMT has not been published previously. Hence, bands at about 940 cm^{-1} (930, 955 cm^{-1}) were assigned to W=O vibrations, while the peaks at 700-900 cm^{-1} (785, 882 cm^{-1}) were explained by the W-O vibrations.

The XRD spectrum of AMT1 does not resemble to any of the published XRD data about AMT [37,38] or the available XRD reference cards of AMT (PDF 00-039-0168 and 04-012-6600). Thus, using Si internal standard we determined the cell parameters of our AMT sample, and refined them with full profile fit. The unit cell of the AMT sample was identified to be orthorhombic ($\alpha = \beta = \gamma = 90°$) with space group Pcca [Nr. 54]. The obtained values for the *a, b, c* cell parameters were 33.438, 17.425, 14.112 Å, respectively, the cell volume was calculated to be 8222.458 $Å^3$, the value of *Z* was 8, and the calculated density was 4.863 g cm^{-3}. The formula of the AMT sample was determined as $(NH_4)_6[H_2W_{12}O_{40}]\cdot 4H_2O$ by TG data (see later). We present the indexed reflections of the AMT1 sample obtained after full profile fit in Table 1, so that they can be used later as a reference.

Thermal decomposition of AMT1 in nitrogen

The first decomposition step (Fig. 4) occurred between 25-200 °C, and it was accompanied by an endothermic heat effect. Here, the crystal water content of ammonium metatungstate evolved, as evidenced by the MS ion current curve of H_2O. The water release happened in two overlapping processes (endothermic DTA peaks at 114 and 139 °C). These correspond altogether to the loss of 4 crystal water molecules (1.6 % and 0.8 % mass losses in the first and second processes, respectively, match the release of ca. 2.7 and 1.3 water molecules). Parallel to this, in the infrared spectrum the intensity of water peaks at 1630 cm^{-1} and 3570 cm^{-1} were slightly decreased (Fig. 2a). The W-O bonds in the solid phase did not change according to infrared spectra. Though, based on this, most probably the metatungstate ion remained intact, the loss of crystal water changed the overall structure of AMT, as the XRD pattern contained much less reflections at 200 °C (Fig. 3a). We could not identify the exact crystal structure at 200 °C with XRD.

In the second decomposition step (250-380°C) in an endothermic reaction most NH_4^+ ions were removed from the structure, and thus NH_3 and H_2O were released (Fig. 4). Accordingly, in the infrared spectrum the intensity of water peaks at 1630 cm^{-1} and 3570 cm^{-1} and of NH_4^+ peaks at 1400 cm^{-1} and 3135 cm^{-1} greatly decreased. The vibrations in the W-O bond region below 1000 cm^{-1} altered significantly (Fig. 2). At 380 °C the XRD pattern shows an

amorphous phase (Fig. 3). This is explained by that when the NH_4^+ ions were removed, the structure of AMT collapsed, and the metatungstate ions, which had been separated previously by NH_4^+ ions, got connected. Consequently, the WO_6 octahedra building up the metatungstate ions changed their position and orientation, and this lead to the formation of an intermediate amorphous phase.

In the third decomposition step (380-500 °C) H_2O and NH_3 were released (Fig. 4). In the infrared spectrum the peaks of water at 1630 cm^{-1} and 3570 cm^{-1} and of NH_4^+ at 1400 cm^{-1} and 3135 cm^{-1} almost completely disappeared (Fig. 2). In this step hexagonal (h-) WO_3 (PDF 33-1387) crystallized from the amorphous phase, accompanied by an exothermic heat effect with a maximum at 421 °C on the DTA curve (Fig. 4).

In the fourth step (500-600 °C) only a small mass loss occurred and tiny amount of water evolved. When the water evolution ended, the metastable h-WO_3 transformed in an exothermic reaction (DTA peak at 548 °C) into the stable monoclinic (m-) modification of WO_3 (PDF 89-4476) [46].

The final mass of the decomposition residue (92.0 mass%) matched well the theoretical value (91.9 mass%) for decomposing $(NH_4)_6[H_2W_{12}O_{40}]\cdot 4H_2O$ into WO_3, thus TG data confirmed the composition of AMT1.

Thermal decomposition of AMT1 in air

In the first decomposition step, there was no difference between the thermal behavior of AMT in air and inert atmospheres (Figs. 5-7). The oxidizing effect of air made a difference only above 250 °C, when the as-released NH_3 started to burn into nitrous oxides, catalyzed by the Pt crucible and/or the as-formed tungsten oxide structure. Among the combustion products of NH_3, the formation of N_2O is favored below 400 °C, while NO forms rather above this temperature [47]. This is clearly shown by the intensity changes in the MS curves of the two gases in the second and third decomposition steps. The combustion of NH_3 is an exothermic reaction, and the generated heat made the DTA peak turn into slightly exothermic (365 °C) at the end of the second decomposition step. In the third decomposition step the exothermic heat effects of the h-WO_3/m-WO_3 transformation (419 °C) and of the NH_3 ignition (441 °C) were added, and thus the DTA peak between 400-450 °C was much sharper in air than in nitrogen.

In air there were no significant differences in the FTIR patterns, compared to nitrogen. In contrast, the XRD pattern recorded in air at 200 °C differed significantly and contained more reflections than in inert atmosphere. Another change in air was that at 500 °C the sample

already contained considerable amount of m-WO_3 besides h-WO_3. As a result, the exothermic DTA peak above 500 °C was much smaller.

Comparison of the morphology, structure and thermal behavior of AMT1 and AMT2

AMT1 and AMT2 differed in their morphology. While AMT1 was built up by 5-50 μm hollow microspheres, AMT2 consisted of 2-10 μm particles, and most of them were aggregated into larger, 10-100 μm blocks.

In contrast to the different morphologies, both FTIR spectra and the XRD patterns of AMT1 and AMT2 were identical. In the FTIR spectra the positions and intensities of the W-O, O-H and N-H bands were the same for both AMT1 and AMT2. Similarly, the 2θ values and relative intensities of the XRD reflections were also identical in the case of the two AMT materials, and AMT2 had the same unit cell as AMT1.

The TG/DTA curves of AMT2 (Fig. 8) were not just similar to AMT1, but basically identical with it. The residual masses for AMT1 and AMT2 in the first, second and third decomposition steps were almost the same, i.e. 97.6 and 97.6 %; 93.5 and 93.4 %; 92.0 and 91.9 %, respectively.

The final mass of the decomposition residue (91.9 mass%) matched the theoretical value (91.9 mass%) for decomposing $(NH_4)_6[H_2W_{12}O_{40}]\cdot 4H_2O$ into WO_3, and not that of $(NH_4)_6[W_{12}O_{39}]\cdot 4H_2O$ (92.4 mass%). Therefore, TG/DTA data also supported that AMT2 was identical with AMT1, and its composition was not $(NH_4)_6[W_{12}O_{39}]\cdot 4H_2O$, as provided by its manufacturer, but $(NH_4)_6[H_2W_{12}O_{40}]\cdot 4H_2O$.

Comparison of the thermal behavior of AMT and APT

Previously AMT [1,33,38,47-52] or a structure close to AMT [38] was said to be a decomposition product of APT at 240 °C. Based on these, it was unknown whether the decomposition of AMT would be the same as the decomposition of APT above 240 °C, or it would differ significantly.

The decomposition of APT includes several steps [1,33,38,47-52]. In inert atmosphere until ca. 170 °C APT loses its crystal water content in an endothermic reaction. Then in the second decomposition step between ca. 170-240 °C, dry NH_3 is released, accompanied by an endothermic heat effect. It was at this point, that previously AMT was reported to form, while

recently it was shown that the intermediate decomposition product of APT here is an ammonium hydrogen paratungstate with the ideal composition of $(NH_4)_6H_4[H_2W_{12}O_{42}]$, from which AMT can be produced by digesting the intermediate by hot water [38]. Then between 240-370 °C both NH_3 and H_2O are released, and an amorphous phase forms in an endothermic reaction. Between 370-450 °C from this phase hexagonal ammonium tungsten bronze (HATB), $(NH_4)_{0.33-x}WO_{3-y}$ or h-WO_3 forms. It is noted that there is no sharp division line between h-WO_3 and HATB. The difference between these two phases is caused mostly by the more oxidized state of tungsten atoms in h-WO_3 and also by the lower occupancy of the hexagonal channels in the case of h-WO_3 [53,54]. Between 500-600 °C the as-formed HATB/h-WO_3 then transforms in an exothermic reaction to the more stable monoclinic tungsten oxide. In air, the decomposition sequence of APT is quite similar. In the oxidizing atmosphere, as a difference the as-released NH_3 starts to burn above 250-300 °C, changing the DTA peaks into exothermic. The exothermic formation of m-WO_3 takes place at 50 °C lower temperature in air than in inert atmosphere.

Our results have shown that below 170-200 °C, similarly APT, AMT lost its crystal water content. A clear difference was that while between 170-240 °C dry NH_3 is released from APT, no dry NH_3 evolution was observed in the case of AMT in this temperature region. The collapse of the starting crystal structure and the formation of an amorphous phase between 250-380 °C were similar in the case of the two materials. The exothermic crystallization of HATB/h-WO_3 and its exothermic transformation into m-WO_3 at elevated temperatures was also similar.

To conclude, the thermal decompositions of APT and AMT are similar; the main difference is that the release of dry NH_3 between 170-240 °C does not take place in the case of AMT.

Conclusions

We have studied the structure, morphology and thermal decomposition of two commercially available ammonium metatungstate (AMT1 and AMT2) materials by SEM, FTIR, XRD and TG/DTA-MS. The need for our research was that there had been no previous studies on the thermal behavior of AMT.

The cell parameters of the AMT1 sample were determined, and its XRD reflections were indexed after full profile fit. It was found, that the XRD patterns and FTIR spectra of both AMT materials, which had different CAS numbers, were basically the same. The samples only differed in their morphology.

The thermal decomposition of AMT involved several steps in inert atmosphere: (i) release of crystal water to get dehydrated AMT between 25-200 °C; (ii) formation of an amorphous phase between 200-380 °C, from which (iii) hexagonal WO_3 formed between 380-500 °C, which then transformed into the more stable m-WO_3 between 500-600 °C. As a difference compared to inert atmosphere, in air the as-formed NH_3 ignited with an exothermic heat effect.

Similar to their XRD patterns and FTIR spectra, the two AMT materials had identical thermal decomposition courses as well. Thermal data confirmed that both AMT1 and AM2 had the formula $(NH_4)_6[H_2W_{12}O_{40}]\cdot 4H_2O$.

The thermal behavior of AMT resembled to the widely studied APT. The main difference between them was the lack of dry NH_3 evolution between 170-240 °C in the case of AMT.

Acknowledgements

I. M. S. thanks for a János Bolyai Research Fellowship of the Hungarian Academy of Sciences and an OTKA-PD-109129 grant.

References

[1] Lassner E, Schubert WD. Tungsten properties, chemistry, technology of the element, alloys, and chemical compounds. New York: Kluwer Academic/Plenum Publishers; 1999.

[2] Hammond C, Straus J, Righettoni M, Pratsinis SE, Hermans I. Nanoparticulate tungsten oxide for catalytic epoxidations. ACS Catal. 2013;3:321-7.

[3] Di Valentin C, Wang F, Pacchioni G. Tungsten oxide in catalysis and photocatalysis: Hints from DFT. Topics Catal. 2013;56:1404-19.

[4] Veith GM, Lupini AR, Pennycook SJ, Alberto V, Prati L, Dudney NJ. Magnetron sputtering of gold nanoparticles onto WO_3 and activated carbon. Catal Today 2007;122:248-53.

[5] Phuruangrat A, Ham DJ, Hong SJ, Thongtem S, Lee JS. Synthesis of hexagonal WO_3 nanowires by microwave-assisted hydrothermal method and their electrocatalytic activities for hydrogen evolution reaction. J Mater Chem. 2010;20:1683-90.

[6] Szilágyi IM, Fórizs B, Rosseler O, Szegedi Á, Németh P, Király P, Tárkányi G, Vajna B, Varga–Josepovits K, László K, Tóth AL, Baranyai P, Leskelä M. WO_3 photocatalysts: influence of structure and composition. J Catal. 2012;294:119-27.

[7] Lin CT, Tsai TH. Solution volume effect of photodegradation by 1-D WO_3 nanorods via microwave-assisted solvothermal heating under the UV irradiation. Asian J Chem. 2013;25:7098-102.

[8] Nandiyanto ABD, Arutanti O, Ogi T, Iskandar F, Kim TO, Okuyama K. Synthesis of spherical macroporous WO_3 particles and their high photocatalytic performance. Chem Eng Sci. 2013;101:523-32.

[9] Liu BX, Wang JS, Li HY, Wu JS, Zhou ML, Zuo TY. Facile synthesis of hierarchical hollow mesoporous Ag/WO_3 spheres with high photocatalytic performance. J Nanosci Nanotech. 2013;13:4117-22.

[10] Karacsonyi E, Baia L, Dombi A, Danciu V, Mogyorosi K, Pop LC, Kovacs G, Cosoveanu V, Vulpoi A, Simon S, Pap Z. The photocatalytic activity of TiO2/WO_3/noble metal (Au or Pt) nanoarchitectures obtained by selective photodeposition. Catal Today 2013;208:19-27.

[11] Szilágyi IM, Saukko S, Mizsei J, Tóth AL, Madarász J, Pokol G. Gas sensing selectivity of hexagonal and monoclinic WO_3 to H_2S. Solid State Sci. 2010;12:1857-60.

[12] Szilágyi IM, Wang L, Gouma PI, Balázsi C, Madarász J, Pokol G. Preparation of hexagonal WO_3 from hexagonal ammonium tungsten bronze for sensing NH_3. Mater Res Bull. 2009;44:505-8.

[13] Balázsi C, Wang L, Zayim EO, Szilágyi IM, Sedlackova K, Pfeifer J, Tóth AL, Gouma PI. Nanosize hexagonal tungsten oxide for gas sensing applications. J Eur Ceram Soc. 2008;28:913-7.

[14] Szilágyi IM, Saukko S, Mizsei J, Király P, Tárkányi G, Tóth AL, Szabó A, Varga-Josepovits K, Madarász J, Pokol G. Controlling the composition of nanosize hexagonal WO_3 for gas sensing. Mater Sci Forum 2008;589:161-5.

[15] Wang L, Pfeifer J, Balázsi C, Szilágyi IM, Gouma PI. Nanostructured hexagonal tungsten oxides for ammonia sensing. Proceedings of SPIE - The International Society for Optical Engineering "Nanosensing: Materials, Devices, and Systems III. 2007,6769:67690E.

[16] Balázsi C, Sedlackova K, Pfeifer J, Tóth AL, Zayim EA, Szilágyi IM, Wang LS, Kalyanasundaram K, Gouma PI. Synthesis and examination of hexagonal Tungsten oxide nanocrystals for electrochromic and sensing applications. NATO Science for

Peace and Security Series C: Environmental Security; Sensors for Environment, Health and Security. 2009:77-91.

[17] Kukkola J, Mohl M, Leino AR, Maklin J, Halonen N, Shchukarev A, Konya Z, Jantunen H, Kordas K. Room temperature hydrogen sensors based on metal decorated WO_3 nanowires. Sens Actuat B. 2013;186:90-5.

[18] Zhang YD, He WW, Zhao HX, Li PJ. Template-free to fabricate highly sensitive and selective acetone gas sensor based on WO_3 microspheres. Vacuum. 2013;95:30-4.

[19] Chromčíková M, Liška M, Lissová M, Mošner P, Koudelka L. Structural relaxation of $PbO–WO_3–P_2O_5$ glasses. J Therm Anal Calorim. 2013;114:947–54.

[20] Shen Y, Zhu H, Huang R, Zhao L, Yan SN. Synthesis and photochromic properties of WO_3 powder induced by oxalic acid. Sci China Ser B-Chem. 2009;52:609-14.

[21] Cai GF, Zhou D, Xiong QQ, Zhang JH, Wang XL, Gu CD, Tu JP. Efficient electroctrochromic materials based on $TiO_2@WO_3$ core/shell nanorod arrays. Solar En Mater Solar Cell. 2013;117:231-8.

[22] Hongjie L, Zhang L. An overview on synthetic methods of benzyl acetate. Eur Chem Bull. 2013;2:272-4.

[23] Blovská V, Bělina P, Šulcová P. Synthesis of tungstate pigments of the formula $MNd_2W_2O_{10}$ (M = Ni, Zn, Mn). J Therm Anal Calorim. 2013;113:83-9.

[24] Łącz A, Pasierb P. Synthesis and properties of $BaCe_{1-x}Y_xO_{3-\delta}–BaWO_4$ composite protonic conductors. J Therm Anal Calorim. 2013;113: 405-12.

[25] Biedunkiewicz A, Szymczyk A, Chrosciechowska J. Oxidation of (Ti,W)C ceramic powders. J Therm Anal Calorim. 2004;77:75-83.

[26] Kano S, Inoue T. Surface softening and hardening of WC-Co using pulsed laser irradiation. Surf Coat Tech. 2006;201:223-9.

[27] Kim HC, Shon IJ, Yoon JK, Doh JM. Consolidation of ultra fine WC and WC-Co hard materials by pulsed current activated sintering and its mechanical properties. Int J Refract Metal Hard Mater. 2007;25:46-52.

[28] Moreno-Castilla C, Alvarez-Merino MA, Carrasco-Marín F, Fierro JLG. Tungsten and tungsten carbide supported on activated carbon: surface structures and performance for ethylene hydrogenation. Langmuir 2001;17:1752-6.

[29] Szymańska-Kolasa A, Lewandowski M, Sayag C, Djéga-Mariadassou G. Comparions of molybdenum carbide for the hydrodesulfurization of dibenzithiophene. CatalToday. 2007;119:7-12.

[30] Szilágyi IM, Madarász J, Pokol G, Hange F, Szalontai G, Varga-Josepovits K, Tóth AL. The effect of K^+ ion doping on the structure and thermal reduction of hexagonal ammonium tungsten bronze. J Therm Anal Calorim. 2009;97:11-8.

[31] Bartha L, Neugebauer J. Aspects of Effective Doping and the Incorporation of Dopant. Int J Refract Metal Hard Mater. 1995;13:1-34.

[32] Pink E, Bartha L. The Metallurgy of Doped/Non-Sag Tunsgten. London: Elsevier; 1989.

[33] van Put JW. Crystallisation and Processing of Ammonium Paratungstate (APT). Int J Refract Metal Hard Mater. 1995;13:61-76.

[34] Bartha L, Kiss BA, Szalay T. Chemistry of tungsten oxide bronzes. Int J Refract Metal Hard Mater. 1995;13:77-91.

[35] Szilágyi IM, Santala E, Heikkilä M, Pore V, Kemell M, Teucher G, Firkala T, Färm E, Nikitin T, Khriachtchev L, Räsänen M, Ritala M, Leskelä M. Photocatalytic properties of WO_3/TiO_2 core-shell nanofibers prepared by electrospinning and atomic layer deposition. Chem Vapor Dep. 2013;19:149-55.

[36] Szilágyi IM, Santala E, Heikkilä M, Kemell M, Nikitin T, Khriachtchev L, Räsänen M, Ritala M, Leskelä M. Thermal study on electrospun polyvinylpyrrolidone/ammonium metatungtate nanofibers: Optimising the annealing conditions for obtaining WO_3 nanofibers. J Therm Anal Calorim. 2011;105:73-81.

[37] Christian JB, Whittingham MS. Structural study of ammonium metatungstate. J Solid State Chem. 2008;181:1782–91.

[38] Fait MJG, Lunk HJ, Feist M, Schneider M, Dann JN, Frisk TA. Thermal decomposition of ammonium paratungstate tetrahydrate under non-reducing conditions Characterization by thermal analysis, X-ray diffraction and spectroscopic methods. Thermochim Acta. 2008;469:12–22.

[39] Prasad RL, Kushwaha A, Szilágyi IM, Kótai L. Solid state thermal degradation behaviour of 1-D coordination polymers of Ni(II) and Cu(II) bridged by conjugated ligand. J Therm Anal Calorim. 2013;114:653-64.

[40] Szilágyi IM, Deák A, Várhelyi jr. C, Madarász J, Pokol G, Gömöry Á, Várhelyi C. Structural and thermal study of assymetric α-dioxime complexes of Co(III) with Cl and methyl-pyridines. Polyhedron. 2010;10:2185-9.

[41] Zhang HY, Xu L, Wang EB, Jiang M, Wu AG, Li Z. Photochromic behavior and luminescent properties of novel hybrid organic–inorganic film doped with Preyssler's

heteropoly acid $H_{12}[EuP_5W_{30}O_{110}]$ and polyvinylpyrrolidone. Mater Lett. 2003;57:1417-22.

[42] Li Y, Li YG, Zhang ZM, Wu Q, Wang EB. A new polyoxotungstate-based $\{W_{72}V_{30}\}$ spherical cage. Inorg Chem Commun. 2009;12:864-7.

[43] Duplyakin VK, Baklanova ON, Chirkova OA, Antonicheva NV, Arbuzov AB, Voitenko NN, Drozdov VA, Likholobov VA. Interaction of nickel hydroxocarbonate, ammonium paramolybdate, and ammonium metatungstate under mechanical activation. Kin Catal. 2010;51:126-30.

[44] Sunita G, Devassy BM, Vinu A, Sawant DP, Balasubramanian VV, Halligudi SB. Synthesis of biodiesel over zirconia-supported isopoly and heteropoly tungstate catalysts. Catal Commun. 2008;9:696-702.

[45] Sarish S, Devassy BM, Böhringer W, Feltcher J, Halligudi SB. Liquid-phase alkylation of phenol with long-chain olefins over WO_x/ZrO_2 solid acid catalysts. J Mol Catal A. 2005;240:123-31.

[46] Szilágyi IM, Pfeifer J, Balázsi C, Tóth AL, Varga-Josepovits K, Madarász J, Pokol G. Thermal stability of hexagonal tungsten trioxide. J Therm Anal Calorim. 2008;94:499-505.

[47] Madarász J, Szilágyi IM, Hange F, Pokol G. Comparative evolved gas analyses (TG-FTIR, TG/DTA-MS) and solid state (FTIR, XRD) studies on thermal decomposition of ammonium paratungstate tetrahydrate (APT) in air. J Anal Appl Pyrol. 2004;72:197-201.

[48] Mansour SAA, Mohamed MA. Thermal decomposition and the creation of reactive solid surfaces. V. The genesis course of the WO_3 catalyst from its ammonium paratungstate precursor. Thermochim Acta. 1988;129:187-96.

[49] French GJ; F R Sale. A re-investigation of the thermal decomposition of ammonium paratungstate. J Mater Sci. 1981;16:3427-36.

[50] Szilágyi IM, Madarász J, Hange F, Pokol G. On-line evolved gas analyses (EGA by TG-FTIR and TG/DTA-MS) and solid state (FTIR, XRD) studies on thermal decomposition and partial reduction of ammonium paratungstate tetrahydrate. Solid State Ionics. 2004;172:583-6.

[51] Szilágyi IM, Madarász J, Hange F, Pokol G. Partial thermal reduction of ammonium paratungstate tetrahydrate. J Therm Anal Calorim. 2007;88:139-44.

[52] Szilágyi IM, Hange F, Madarász J, Pokol G. In situ HT-XRD study on the formation of hexagonal ammonium tungsten bronze by partial reduction of ammonium paratungstate tetrahydrate. Eur J Inorg Chem. 2006;17:3413-18.

[53] Szilágyi IM, Sakó I, Király P, Tárkányi G, Tóth AL, Szabó A, Varga-Josepovits K, Madarász J, Pokol G. Phase transformations of ammonium tungsten bronzes. J Therm Anal Calorim. 2009;98:707-16.

[54] Szilágyi IM, Madarász J, Király P, Tárkányi G, Tóth AL, Szabó A, Varga-Josepovits K, Pokol G. Stability and controlled composition of hexagonal WO_3. Chem Mater. 2008;20:4116-25.

Tables

Table 1. Powder XRD data of ammonium metatungstate hydrate, $(NH_4)_6[H_2W_{12}O_{40}]\ 4H_2O$ obtained after full profile fit (LOI(c) = 7.86; Orthorhombic; S.G.= Pcca [54]; a_0 = 33.438 Å, b_0 =17.425 Å, c_0 =14.112 Å; MAC=128.89 (CuKα); D_x = 4.863 g cm^{-3}; Z = 8; V = 8222.46 $Å^3$; Internal standard: Si)

Nr.	d/ Å	2θ/ °	Rel. Int./ %	h	k	l
1	10.420	8.485	4.2	1	1	1
2	9.170	9.645	100.0	2	1	1
3	8.712	10.153	14.6	0	2	0
4	8.359	10.583	10.8	4	0	0
5	7.817	11.319	0.6	3	1	1
6	7.537	11.742	0.7	4	1	0
7	7.238	12.229	0.3	1	2	1
8	6.777	13.064	0.7	2	2	1
9	6.648	13.318	0.2	4	1	1
10	6.501	13.622	1.0	2	0	2
11	6.173	14.349	0.5	3	2	1
12	6.091	14.543	2.0	2	1	2
13	6.032	14.686	3.4	4	2	0
14	5.710	15.520	3.5	5	1	1
15	5.641	15.711	3.7	3	1	2
16	5.547	15.979	2.7	4	2	1
17	5.487	16.155	6.6	2	3	0
18	5.392	16.440	17.5	4	0	2
19	5.303	16.718	4.2	1	3	1
20	5.210	17.018	2.2	2	2	2
21	5.114	17.342	22.5	2	3	1
22	4.968	17.853	27.3	6	1	1

Nr.	d/ A°	2 θ / °	Rel. Int./ %	h	k	l
51	3.322	26.841	5.0	9	2	1
52	3.303	26.999	13.1	3	1	4
53	3.242	27.513	4.5	5	4	2
54	3.237	27.552	1.0	3	5	1
55	3.230	27.613	4.0	9	1	2
56	3.209	27.799	5.0	2	2	4
57	3.195	27.923	19.0	4	1	4
58	3.182	28.045	14.0	1	4	3
59	3.138	28.442	12.3	7	4	1
60	3.120	28.607	6.0	5	0	4
61	3.111	28.695	3.0	1	5	2
62	3.086	28.930	4.0	6	4	2
63	3.072	29.064	5.5	3	4	3
64	3.057	29.217	12.4	6	3	3
65	3.048	29.301	5.0	10	2	1
66	3.019	29.590	2.0	5	5	1
67	2.977	30.015	2.0	10	1	2
68	2.938	30.428	2.8	5	2	4
69	2.928	30.526	3.4	7	4	2
70	2.911	30.717	3.2	3	3	4
71	2.839	31.517	18.8	10	3	1
72	2.831	31.606	8.0	5	5	2

23	4.920	18.029	2.1	3	2	2
24	4.854	18.278	1.9	5	0	2
25	4.770	18.602	0.4	4	3	0
26	4.585	19.360	15.6	4	2	2
27	4.500	19.728	1.6	1	1	3
28	4.445	19.977	9.6	1	3	2
29	4.383	20.263	15.4	2	1	3
30	4.356	20.387	8.3	0	4	0
31	4.206	21.125	5.4	3	1	3
32	4.188	21.216	11.0	5	3	1
33	4.131	21.514	0.8	1	4	1
34	4.064	21.868	6.3	8	1	0
35	4.015	22.138	4.1	7	2	1
36	3.991	22.278	3.6	4	1	3
37	3.952	22.500	6.5	4	3	2
38	3.899	22.806	1.9	3	4	1
39	3.863	23.022	10.1	4	4	0
40	3.769	23.609	3.3	8	2	0
41	3.725	23.892	7.3	5	3	2
42	3.709	23.991	3.0	4	2	3
43	3.684	24.157	2.4	1	4	2
44	3.596	24.758	9.6	8	0	2
45	3.571	24.934	11.3	2	3	3
46	3.534	25.202	5.3	5	4	1
47	3.522	25.288	9.3	8	1	2
48	3.389	26.301	10.9	4	4	2
49	3.364	26.500	2.0	3	0	4
50	3.335	26.732	5.5	6	4	1

73	2.813	31.817	7.6	11	2	1
74	2.804	31.914	3.0	2	6	1
75	2.792	32.061	3.5	11	0	2
76	2.761	32.428	13.5	7	5	1
77	2.757	32.481	5.0	11	1	2
78	2.725	32.862	1.5	6	5	2
79	2.706	33.111	2.4	2	4	4
80	2.696	33.232	2.0	8	0	4
81	2.686	33.364	4.2	0	6	2
82	2.681	33.428	3.0	10	3	2
83	2.664	33.639	2.9	8	1	4
84	2.655	33.757	8.0	4	5	3
85	2.652	33.793	5.0	10	4	0
86	2.624	34.170	6.3	9	4	2
87	2.618	34.257	5.3	5	6	1
88	2.610	34.355	7.0	3	2	5
89	2.601	34.481	4.5	10	2	3
90	2.575	34.836	2.5	6	6	0
91	2.564	35.003	2.6	12	1	2
92	2.558	35.076	2.5	9	0	4
93	2.550	35.197	2.3	7	3	4
94	2.531	35.465	1.8	9	1	4
95	2.516	35.683	6.6	11	3	2
96	2.512	35.740	3.5	12	3	0
97	2.492	36.046	8.3	5	2	5
98	2.484	36.160	2.0	12	2	2
99	2.473	36.335	4.6	1	5	4
100	2.464	36.459	4.8	1	6	3

Figures

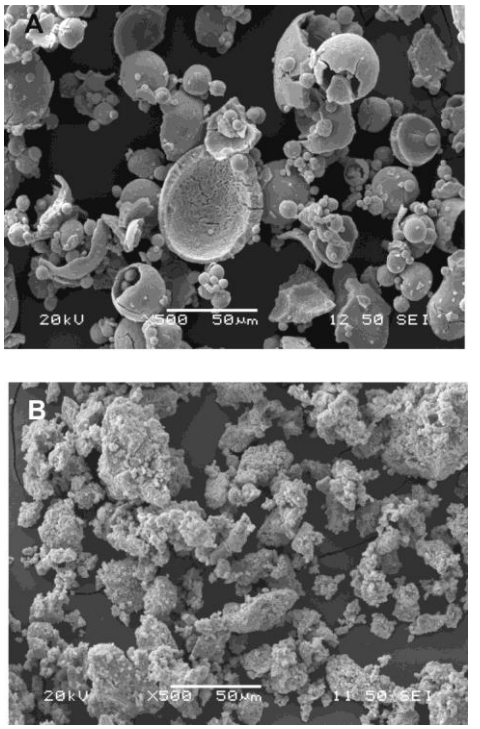

Figure 1. SEM images of (a) AMT1 and (b) AMT2

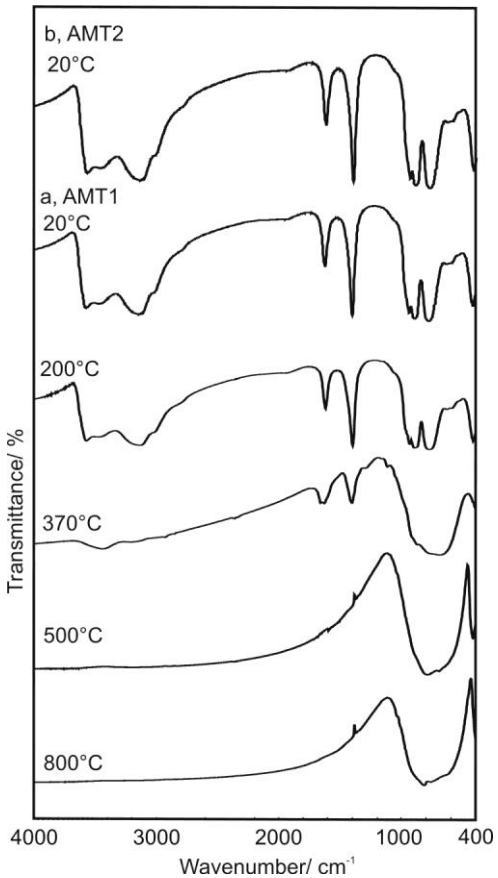

Figure 2. FTIR spectra of (a) AMT1 and its thermal decomposition products in nitrogen and (b) AMT2

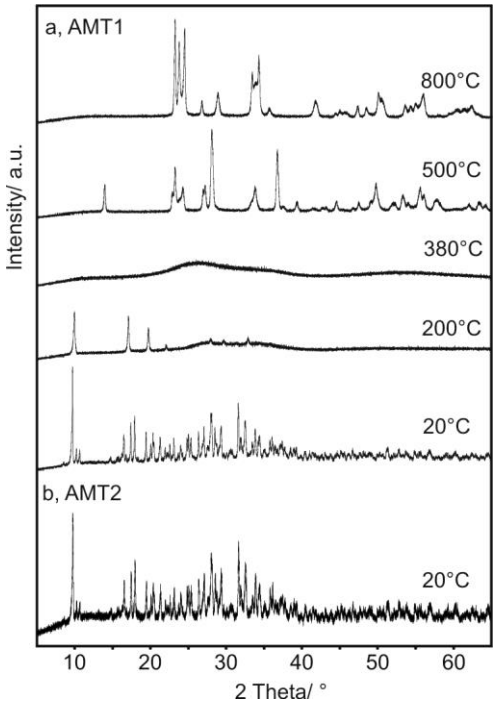

Figure 3. XRD patterns of (a) AMT1 and its thermal decomposition products in nitrogen and (b) AMT2

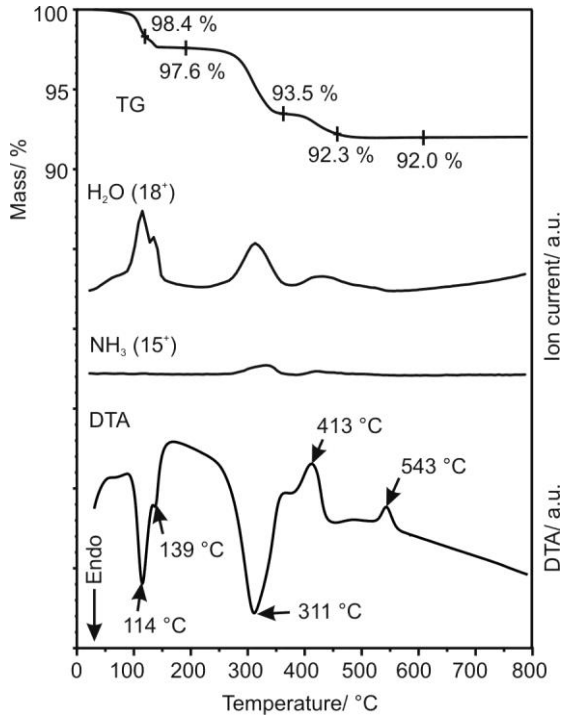

Figure 4. TG/DTA and evolved gas analytical MS ion current curves of the thermal decomposition of AMT1 in nitrogen

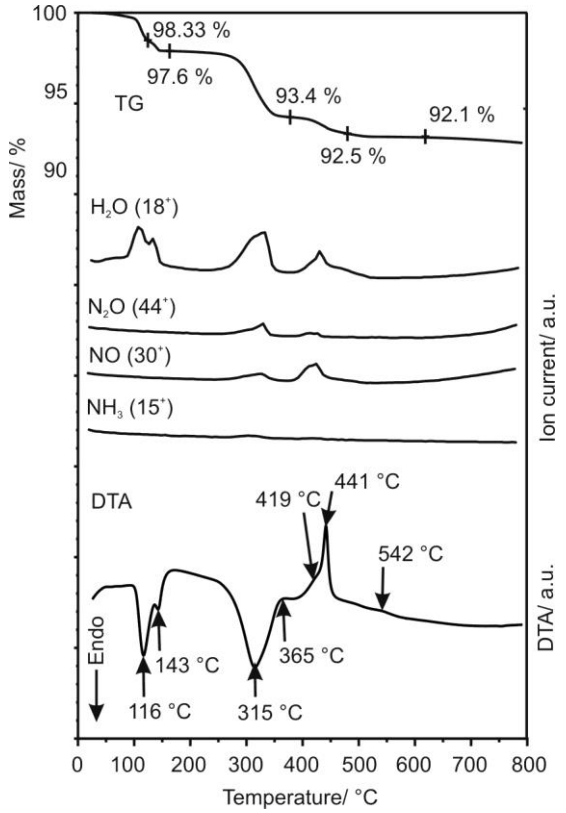

Figure 5. TG/DTA and evolved gas analytical MS ion current curves of the thermal decomposition of AMT1 in air

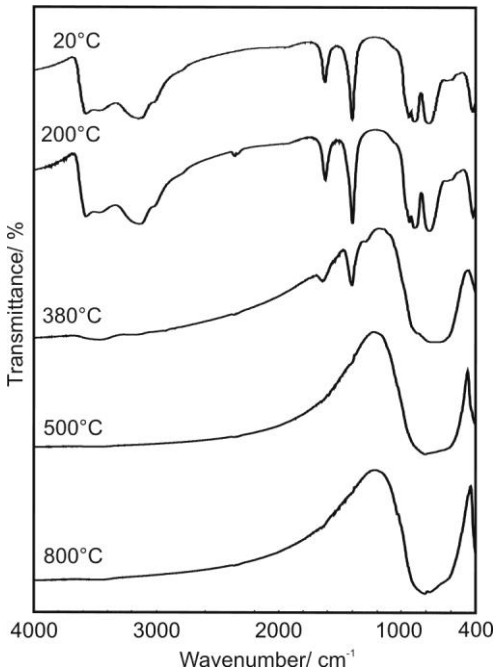

Figure 6. FTIR spectra of the thermal decomposition products of AMT1 in air

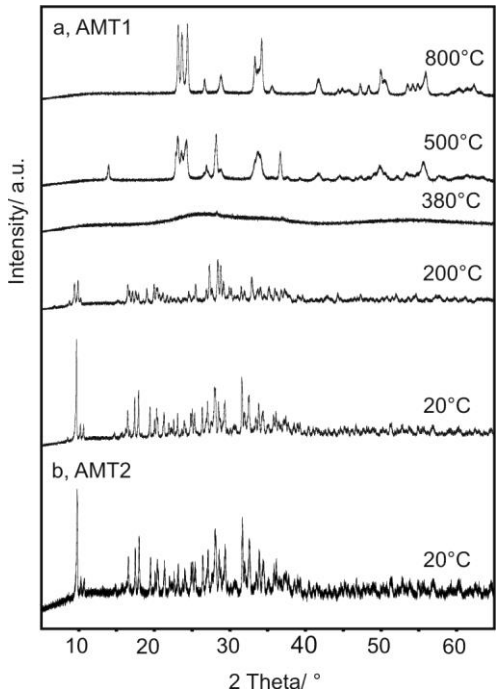

Figure 7. XRD patterns of the thermal decomposition products of AMT1 in air

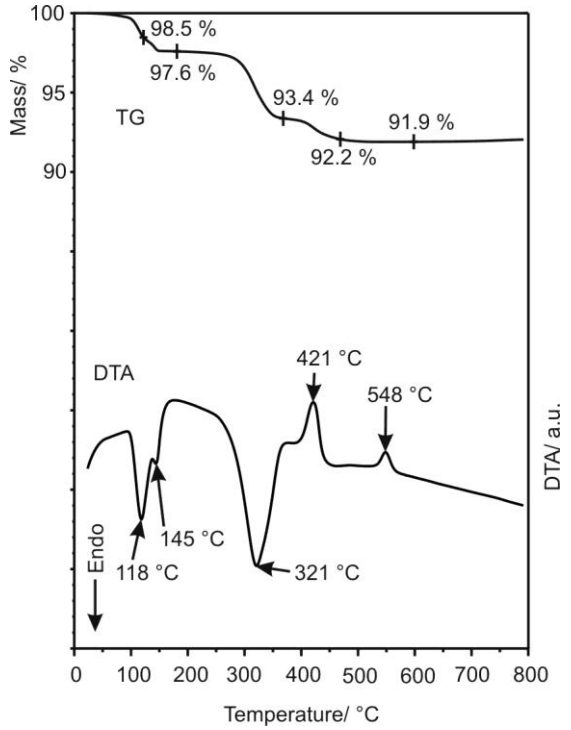

Figure 8. TG/DTA curves of the thermal decomposition of AMT2 in nitrogen